

Supporting Information for

Strongly Coupled Ag/Sn-SnO₂ Nanosheets toward CO₂ Electroreduction to Pure HCOOH Solutions at Ampere-Level Current

Min Zhang¹, Aihui Cao², Yucui Xiang¹, Chaogang Ban¹, Guang Han^{3,4,*}, Junjie Ding¹, Li-Yong Gan^{1,4,5,*}, and Xiaoyuan Zhou^{1,4,5,*}

¹ College of Physics and Center of Quantum Materials and Devices, Chongqing University, Chongqing 401331, P. R. China

² State Key Laboratory of Structural Chemistry, Fujian Institute of Research on the Structure of Matter, Chinese Academy of Sciences (CAS), Fuzhou 350002, P. R. China

³ College of Materials Science and Engineering, Chongqing University, Chongqing 400044, P. R. China

⁴ Institute of New Energy Storage Materials and Equipment, Chongqing 401135, P. R. China

⁵ State Key Laboratory of Coal Mine Disaster Dynamics and Control, Chongqing University, Chongqing 400044, P. R. China

*Corresponding authors. E-mail: xiaoyuan2013@cqu.edu.cn (Xiaoyuan Zhou); ganly@cqu.edu.cn (Li-Yong Gan), guang.han@cqu.edu.cn (Guang Han)

S1 Experimental Procedures

S1.1 Characterization

Powder X-ray diffraction (PXRD) patterns were recorded on an Empyrean X-ray diffractometer at 40 kV and 40 mA with Cu K α radiation in 2 θ ranging from 10° to 80°. Field emission scanning electron microscopy (FESEM) was performed on a Quattro S microscope operated at 5 kV. Transmission electronic microscopy (TEM) and high-resolution TEM (HRTEM) equipped with energy dispersive X-ray spectrometer (EDX) were conducted on a Talos-F200S microscope operated at 200 kV. X-ray photoelectron spectroscopy (XPS) and Ultraviolet Photoelectron Spectrometer (UPS) analyses were performed on a Thermo Fisher Scientific XPS ESCALAB 250Xi instrument with an Al-K α (1486.8 eV) X-ray source. The X-ray absorption spectra of Ag and Sn K-edge (XANES and EXAFS experiments) were carried out in fluorescence mode at the BL14W1 beamline of the Shanghai Synchrotron Radiation Facility (SSRF), China. The EXAFS raw data were then background-subtracted, normalized and Fourier transformed by the standard procedures with the IFEFFIT package. Operando attenuated total reflection-infrared (ATR-IR) spectra were recorded on the IRTracer100 instrument. ¹H NMR was conducted on AVANCE NEO 400 evolution with DMSO as internal standard.

S1.2 Electrochemical Measurements

During the electrolysis, gaseous products were detected by an on-line gas chromatography (GC) (Agilent 7820A) equipped with a molecular sieve 5 Å and two porapak Q columns continuously. The concentration of H₂ and CO was analyzed by a thermal conductivity detector (TCD) and a flame ionization detector (FID), respectively. The quantification of gaseous products was carried out using a conversion factor derived from the standard calibration gases. Liquid products were collected at the end of each electrocatalysis and analyzed by ¹H NMR (Agilent

DD2-400). For the NMR, 0.5 mL of the catholyte was mixed with 0.1 mL of D₂O containing dimethyl sulfoxide (DMSO, 10 ppm) as the internal standard. The concentration of formate was quantitatively determined from its NMR peak area relative to that of the internal standard using the calibration curve from a series of standard formate solutions.

The half-cell cathodic energy efficiency (CEE) was calculated as follows:

$$\text{CEE} = (1.23 - E_{\text{formate}}) / (1.23 - E_{\text{applied}}) \times \text{FE}_{\text{formate}} \times 100\%$$

where $E_{\text{formate}} = -0.2$ V vs. RHE is the thermodynamic potential of CO₂ reduction to formate. $\text{FE}_{\text{formate}}$ is the Faradaic efficiency of formate production. E_{applied} is the applied potential vs. RHE.

The electrochemical impedance spectroscopy (EIS) was recorded at -0.73 V with the frequency ranging from 0.1 to 10⁵ Hz at the AC amplitude of 5 mV.

The adsorption of OH⁻ as a surrogate of CO₂*⁻ was examined through a cathodic LSV scan between -0.4 and 0.38 V in Ar-saturated aqueous 0.1 M KOH solution at a scan rate of 10 mV s⁻¹.

Electrochemically active surface area (ECSA) was obtained by measuring the electrochemical double-layer capacitance from the scan-rate dependence of CVs in a potential range of -0.18 to -0.08 V. The electrochemical impedance spectroscopy (EIS) was recorded at -0.73 V with the frequency ranging from 0.1 to 10⁵ Hz at the AC amplitude of 5 mV.

For ATR-IR measurements, the loaded Ag/Sn-SnO₂ (or Sn-SnO₂) electrode was used as the working electrode, along with Ag/AgCl as the reference electrode, and platinum wire as the counter electrode.

S2 Supplementary Figures and Tables

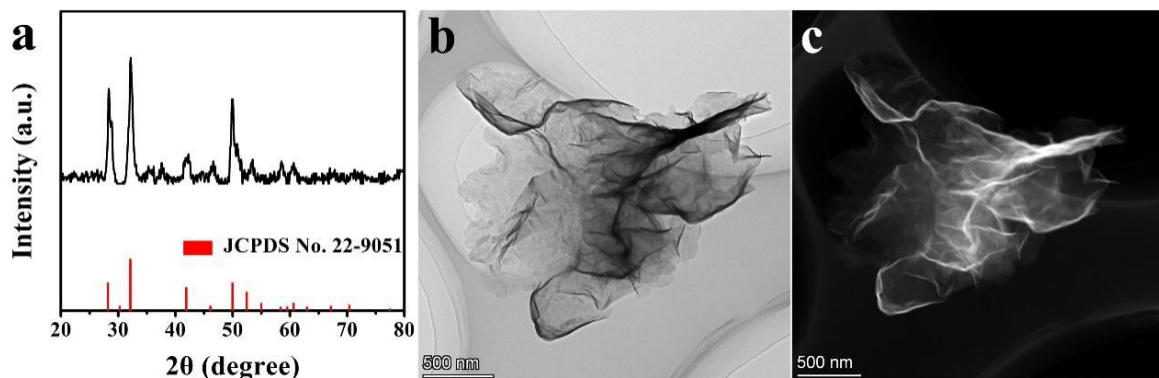


Fig. S1 Characterization of SnS₂ NSs: (a) XRD pattern; (b) TEM image; (c) HAADF-STEM image

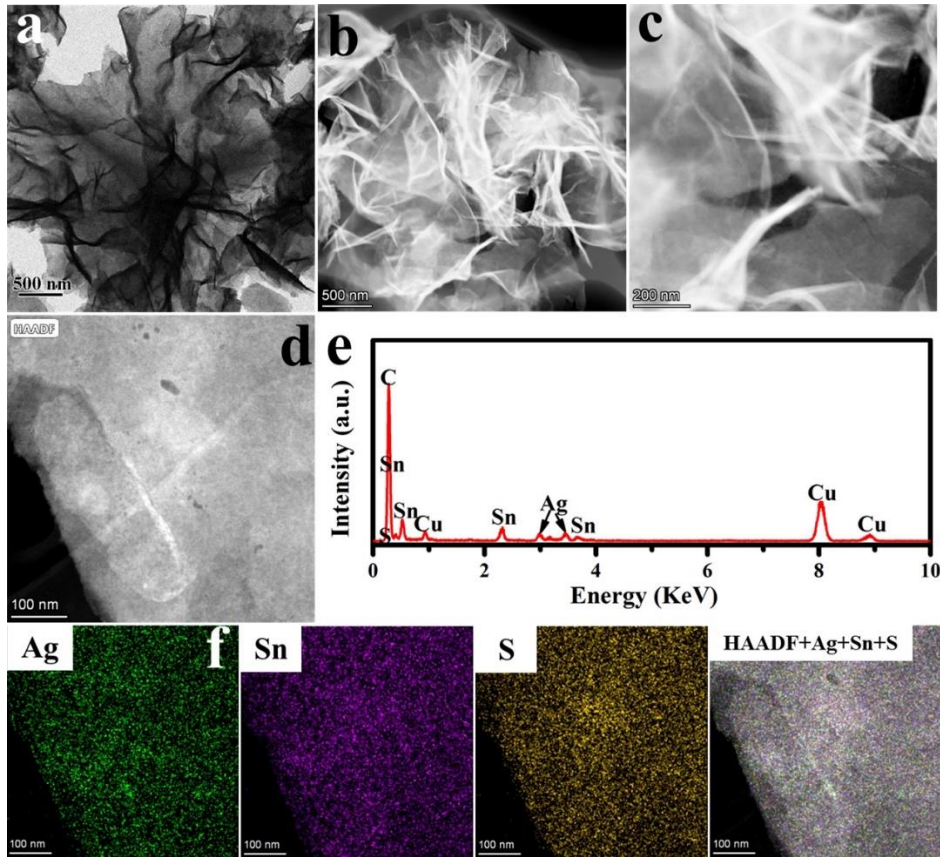


Fig. S2 Characterization of Ag-SnS₂ NSs: (a) TEM image; (b, c) STEM images; (d) HAADF-STEM image; (e) corresponding EDX spectrum; (f) EDX mapping images

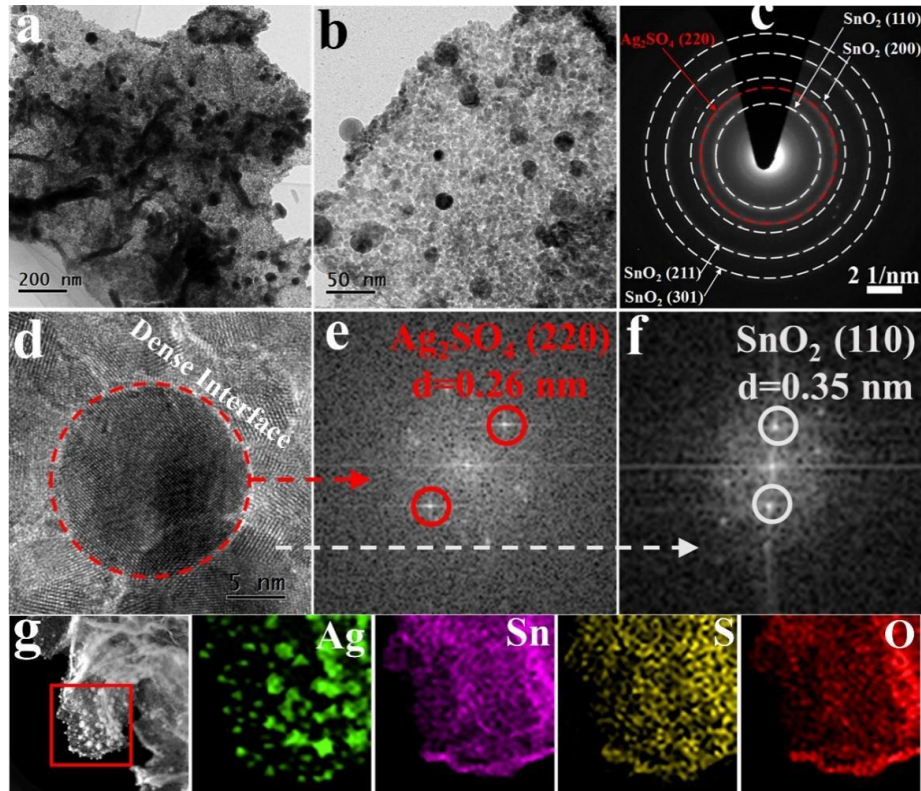


Fig. S3 Characterization of Ag₂SO₄/SnO₂ NSs: (a, b) TEM images; (c) SAED pattern; (d) HRTEM image; (e, f) corresponding FFT patterns; (g) HAADF-STEM and EDX mapping images

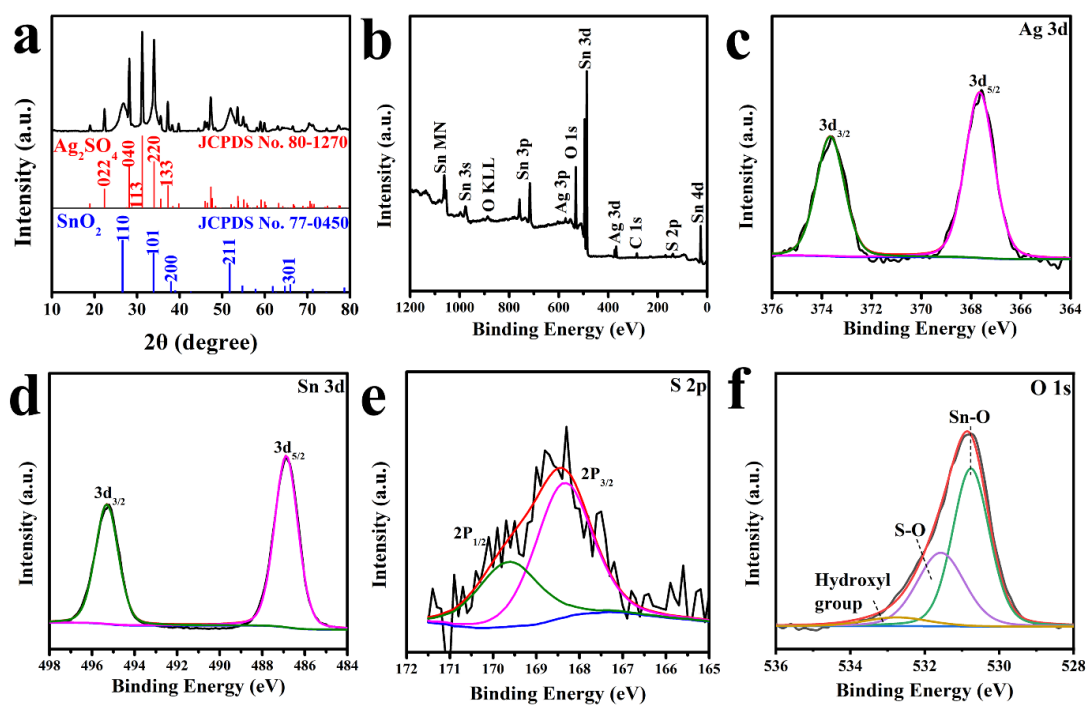


Fig. S4 Characterization of $\text{Ag}_2\text{SO}_4/\text{SnO}_2$ NSs: (a) PXRD pattern; XPS spectra of (b) full spectrum, (c) Ag 3d spectrum, (d) Sn 3d spectrum, (e) S 2p spectrum, (f) O 1s spectrum.

PXRD pattern exhibits that all the diffraction peaks of the product can be indexed to the Ag_2SO_4 and SnO_2 phase (**Fig. S4a**). The surface chemical state and composition of the $\text{Ag}_2\text{SO}_4/\text{SnO}_2$ NSs were further characterized by X-ray photoelectron spectroscopy (XPS). As shown in **Fig. S4b**, there are a series of peaks corresponding to Sn, Ag, O, C, and S elements in the survey spectrum of the $\text{Ag}_2\text{SO}_4/\text{SnO}_2$ NSs. Ag 3d spectra showed Ag 3d_{5/2} and Ag 3d_{3/2} peaks at binding energies of 367.5 and 373.5 eV, respectively, indicating the metallic Ag^+ characteristics of sample surfaces (**Fig. S4c**). **Fig. S4d** shows the Sn 3d spectrum, in which peaks at 494.6 and 486.3 eV correspond to Sn 3d_{3/2} and 3d_{5/2} orbitals of Sn^{4+} . In the S 2p spectra (**Fig. S4e**), two splitting peaks around 168.6 and 169.8 eV are assigned to S^{6+} 2p_{3/2} and 2p_{1/2} orbitals. In the O 1s spectrum (**Fig. S4f**), the peak at 531.9 eV is associating with the S-O bonds in SO_4^{2-} species, and the peak at 529.9 eV is assigned to the Sn-O bonds. In addition, a peak around 533 eV was also detected which is ascribed to hydroxyl groups.

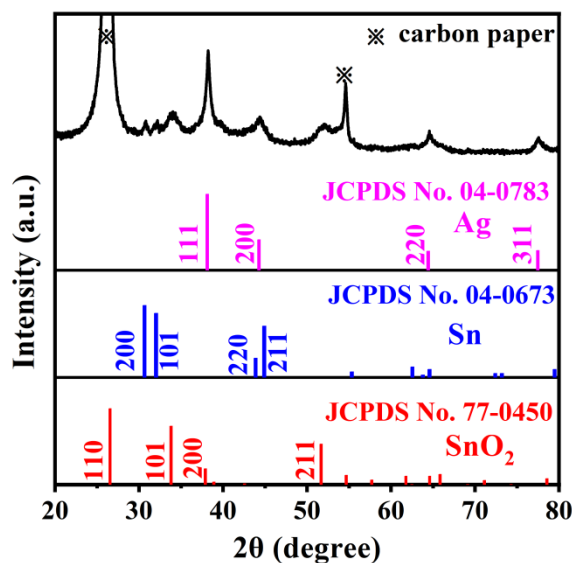


Fig. S5 XRD pattern of Ag/Sn- SnO_2 NSs

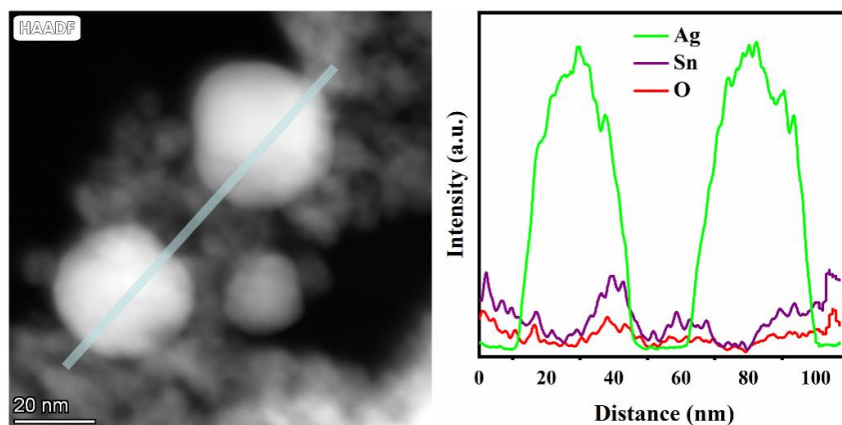


Fig. S6 HAADF-STEM image and corresponding EDX line scans of Ag/Sn-SnO₂ NSs

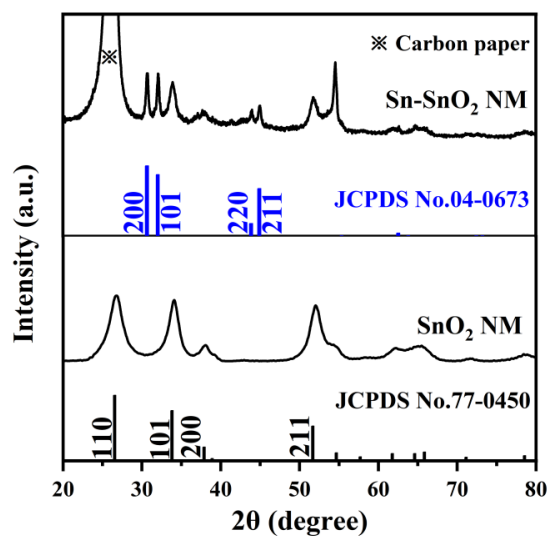


Fig. S7 XRD patterns of SnO₂ NSs and Sn-SnO₂ NSs

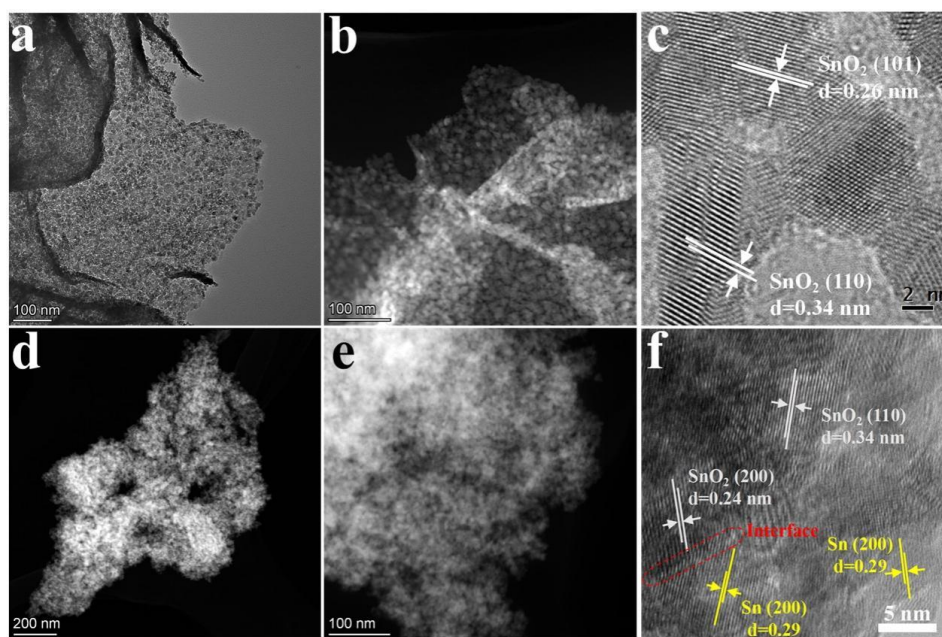


Fig. S8 Characterization of SnO₂ NSs and derived Sn-SnO₂ NSs: (a) TEM image, (b) HAADF-STEM image, (c) HRTEM image of SnO₂ NSs; (d, e) HAADF-STEM images, (f) HRTEM image of Sn-SnO₂ NSs

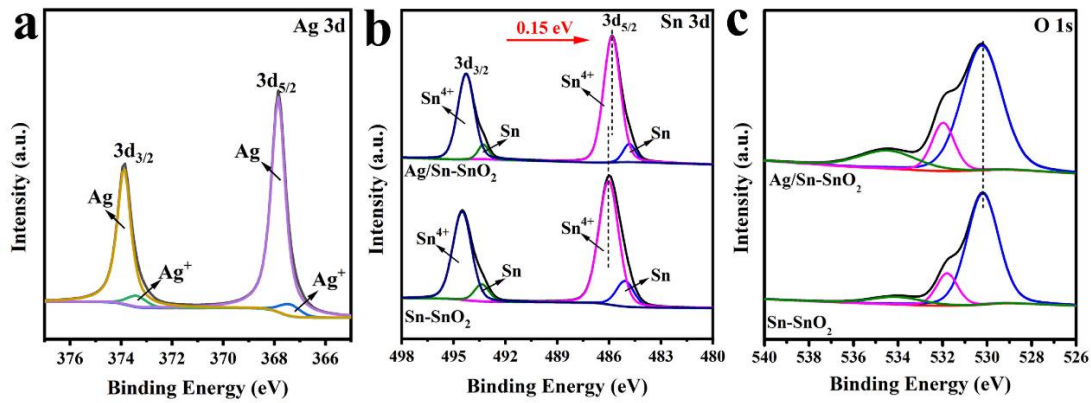


Fig. S9 High-resolution XPS spectra: (a) Ag 3d of Ag/Sn-SnO₂ NSs; (b) Sn 3d of Ag/Sn-SnO₂ NSs and Sn-SnO₂ NSs; (c) O 1s of Ag/Sn-SnO₂ NSs and Sn-SnO₂ NSs

The O 1s spectra for Ag/Sn-SnO₂ NSs and Sn-SnO₂ NSs were resolved into three peaks at the binding energies of 529.4, 531.6, and 534.2 eV, corresponding to the lattice oxygen of Sn-O, oxygen atoms adjacent to O_{vacs}, and the adsorbed oxygen (O_{ads}), respectively (**Fig. S9c**).

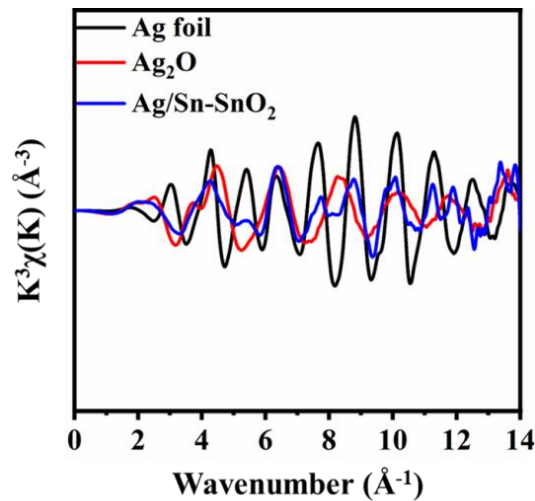


Fig. S10 Ag K-edge EXAFS oscillations of Ag foil, Ag₂O and Ag/Sn-SnO₂

The oscillation curves of Ag K-edge for Ag/Sn-SnO₂ in the K range of 0–14.0 Å⁻¹ also displayed obvious decrease in oscillation intensity with respect to Ag foil and Ag₂O (**Fig. S10**), indicating the existence of two silver phases.

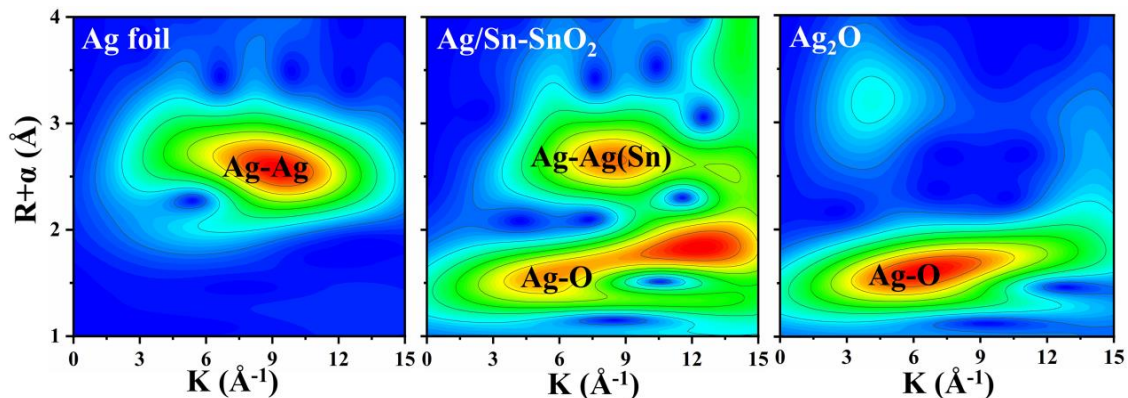


Fig. S11 Wavelet transform EXAFS of Ag of Ag foil, Ag/Sn-SnO₂, and Ag₂O

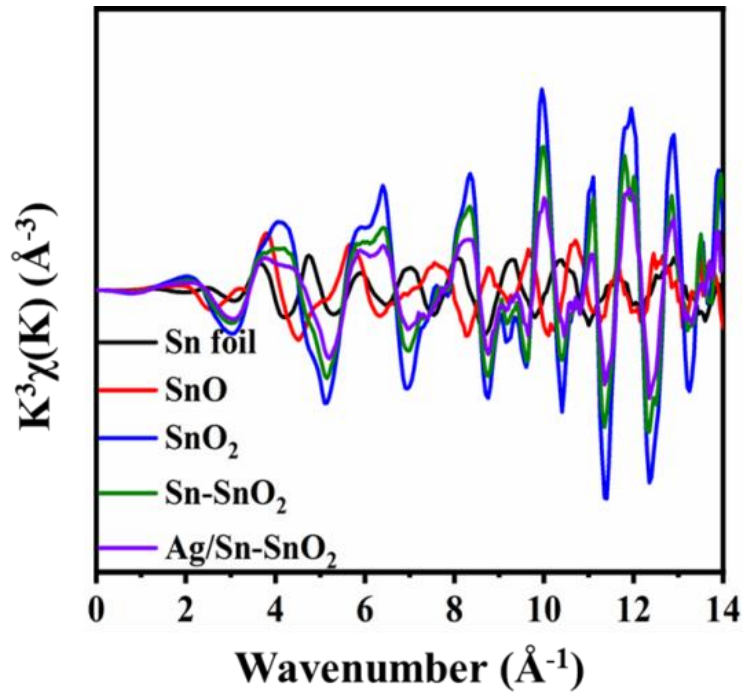


Fig. S12 Sn K-edge EXAFS oscillations of Sn foil, SnO₂, Sn-SnO₂, Ag/Sn-SnO₂ and SnO

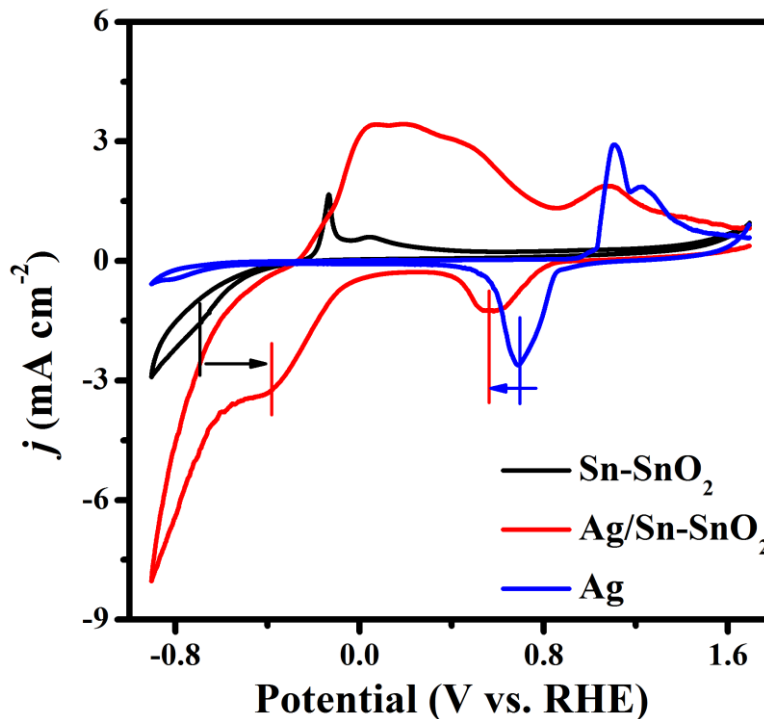


Fig. S13 The Sn⁴⁺/Sn and Ag⁺/Ag reduction waves of Ag/Sn-SnO₂ in cyclic voltammetry curves

The cyclic voltammetry (CV) test was first conducted in an Ar-saturated 0.5 M KHCO₃ electrolyte to investigate the Ag and Sn-SnO₂ interaction. As shown in **Fig. S13**, the Sn⁴⁺ to Sn reduction peak shifted from -0.39 V (for Sn-SnO₂) to -0.37 V (for Ag/Sn-SnO₂), while the Ag⁺/Ag reduction peak shifted from 0.75 V (for Ag powder) to 0.63 V (for Ag/Sn-SnO₂), suggesting that the interphase electron transfer from Ag to Sn atoms, during which Sn atoms as electron acceptor became electron enrichment.

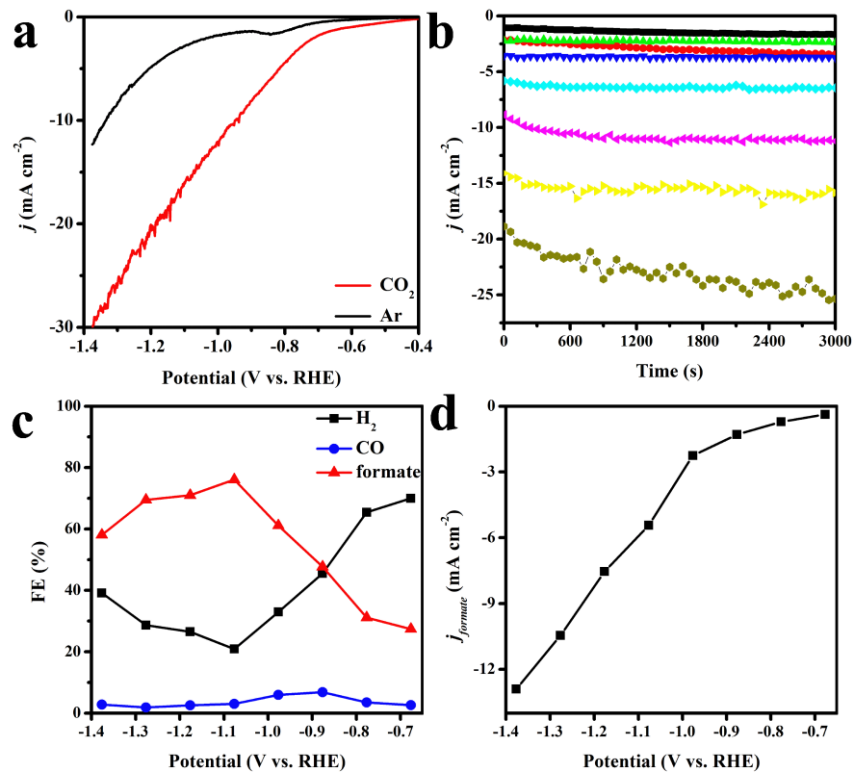


Fig. S14 Electrocatalytic CO₂RR performance of Sn-SnO₂ NSs in CO₂-saturated 0.5 M KHCO₃: (a) Polarization curves in Ar- or CO₂-saturated solution; (b) Total current densities at designated potentials; (c) FE for formate, CO and H₂; (d) Partial current densities of formate

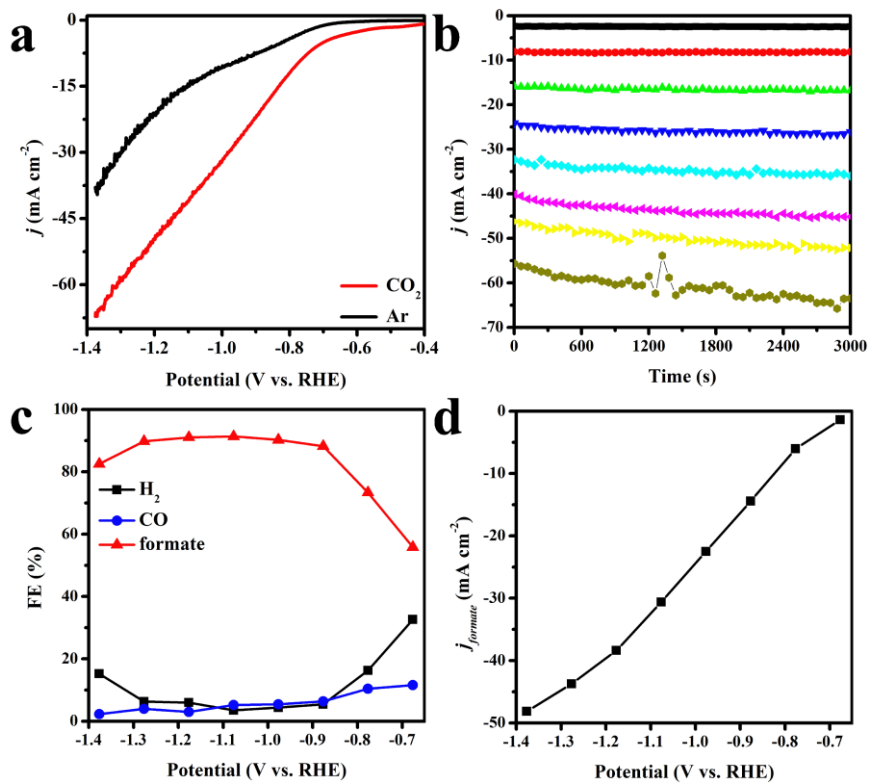


Fig. S15 Electrocatalytic CO₂RR performance of Ag/Sn-SnO₂ NSs in CO₂-saturated 0.5 M KHCO₃: (a) Polarization curves in Ar- or CO₂-saturated solution; (b) Total current densities at designated potentials; (c) FE for formate, CO and H₂; (d) Partial current densities of formate

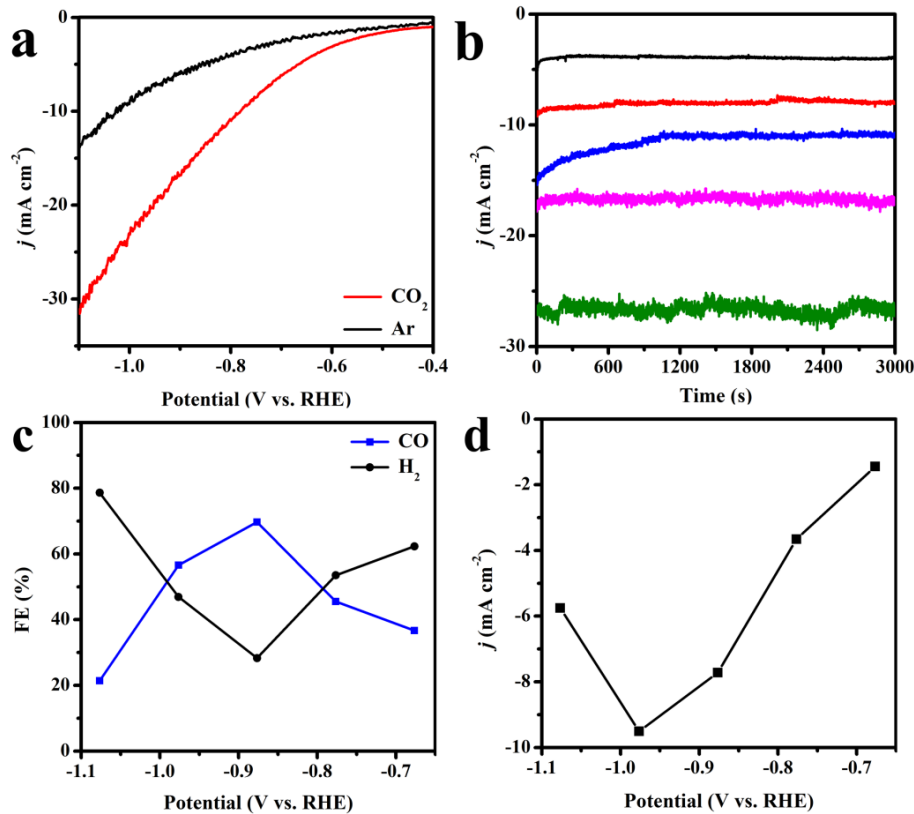


Fig. S16 Electrocatalytic CO₂RR performance of Ag powder in CO₂-saturated 0.5 M KHCO₃: (a) Polarization curves in Ar- or CO₂-saturated solution; (b) Total current densities at designated potentials; (c) FE for CO and H₂; (d) Partial current densities of CO

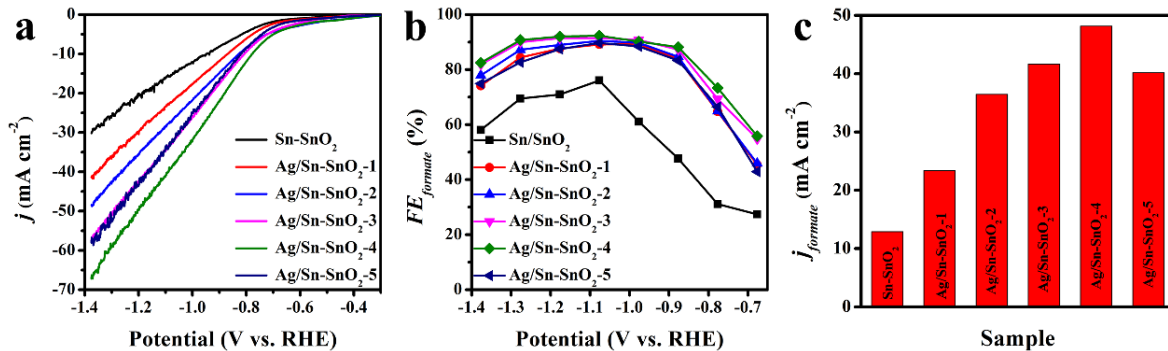


Fig. S17 Electrocatalytic CO₂RR performance of Ag powder in CO₂-saturated 0.5 M KHCO₃: (a) Polarization curves in CO₂-saturated solution; (b) FE for formate; (c) Partial current densities of formate

Where the content of Ag in Ag/Sn-SnO₂ was indirectly controlled by changing the concentration of Ag⁺ in the ion exchange experiment. Firstly, 0.1 g of SnS₂ NSs were dispersed in 80 mL of ethanol with sonication for 30 min. Then, 20 mL of ethanol solution of AgNO₃ (0.12, 0.24, 0.36, 0.48, 0.5 mM, name 1, 2, 3, 4, 5) was added to the above mixture with magnetic stirring for 12 h at 60 °C. Subsequently, the Ag⁺-exchanged SnS₂ NSs was collected, washed, and dried, and it was further calcined at 500 °C for 2 h in O₂ with a heating rate of 5 °C min⁻¹. Finally, Ag/Sn-SnO₂-X (X=1, 2, 3, 4, 5) were obtained via an in situ electrochemical self-reconstruction process.

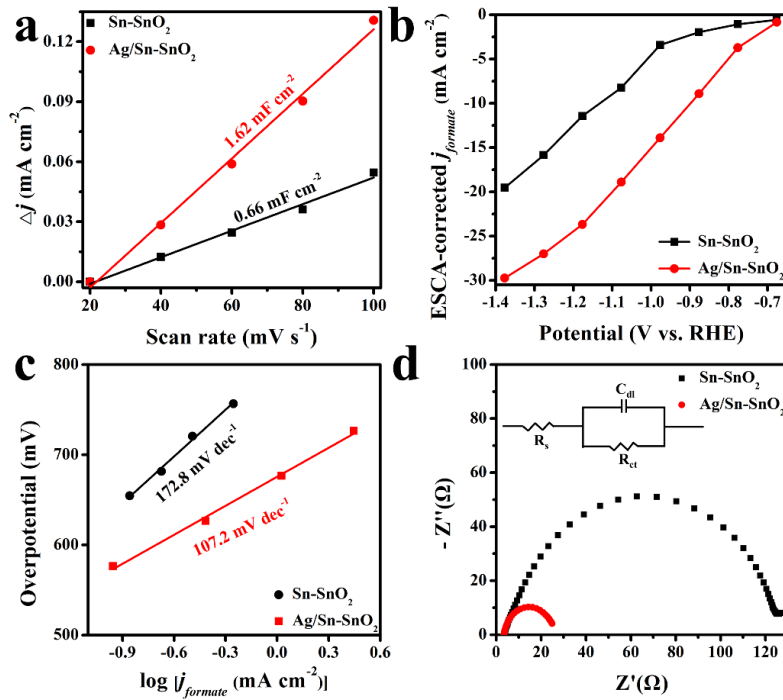


Fig. S18 The Sn-SnO₂ NSs and Ag/Sn-SnO₂ NSs for electrocatalytic CO₂ reduction: (a) ESCAs; (b) ESCAs-normalized formate partial current density; (c) Tafel plots; (d) Nyquist plots (insert is simplified randles circuit)

In a simplified Randles circuit, R_s and R_{ct} represent the solution resistance and charge transfer resistance, respectively. C_{dl} element models the double-layer capacitance. The kinetics for Faradaic CO₂RR is determined by charge transfer resistance (R_{ct}).

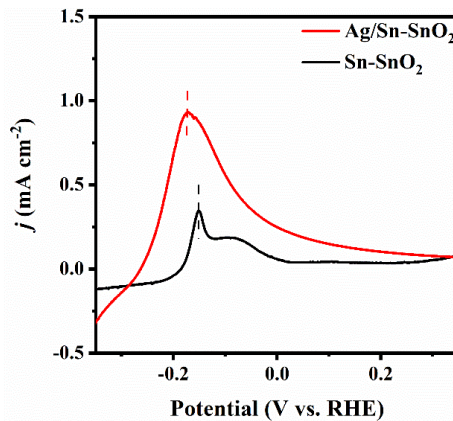


Fig. S19 LSV curves of Ag/Sn-SnO₂ NSs and Sn-SnO₂ NSs in Ar-saturated 0.1 M KOH electrolyte

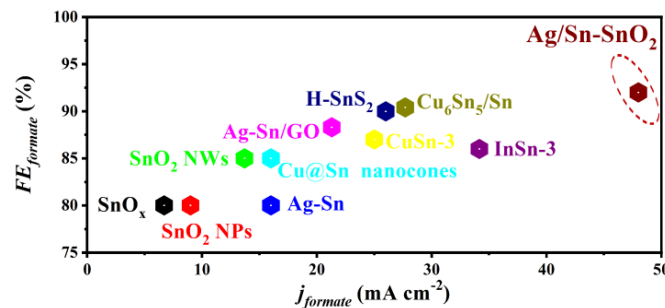


Fig. S20 Comparison of the performance of Ag/Sn-SnO₂ NSs with other Sn-based catalysts of H-type reactor

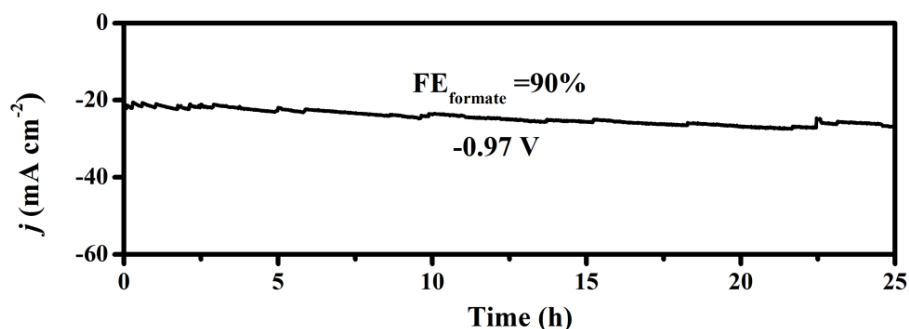


Fig. S21 Stability test for Ag/Sn-SnO₂ NSs at a potential of -0.97 V vs. RHE

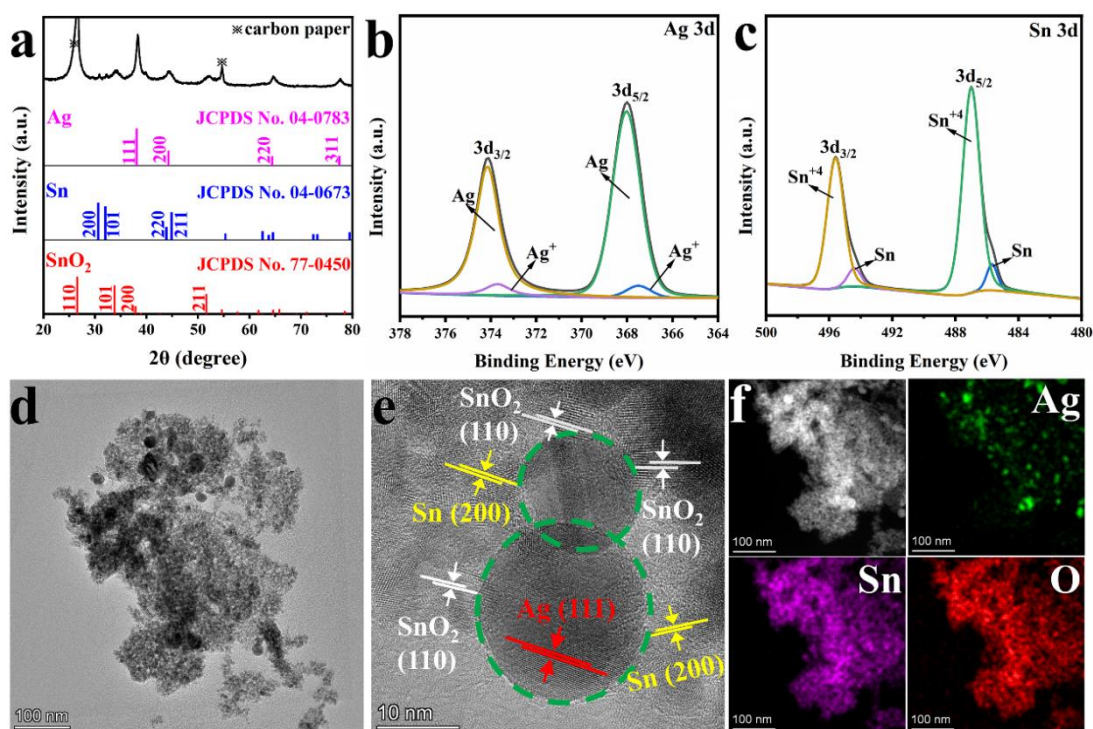


Fig. S22 The recycled Ag/Sn-SnO₂ NSs after stability test: (a) XRD pattern; high-resolution XPS spectra of (b) Ag 3d, and (c) Sn 3d; (d) TEM image; (e) HRTEM image; (f) corresponding EDS mapping images

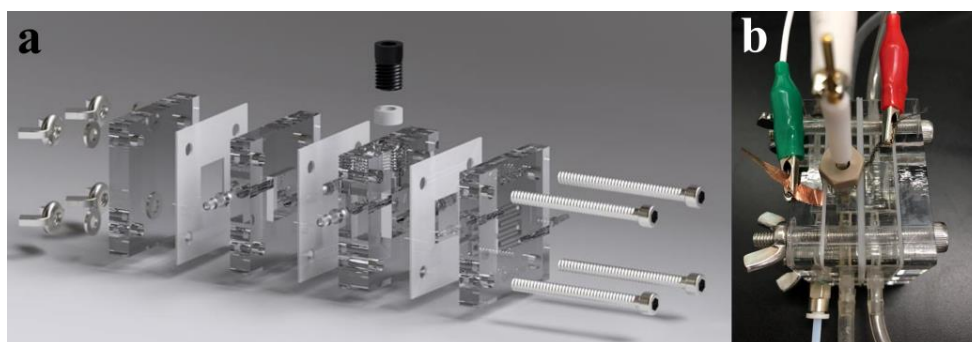


Fig. S23 Flow-type reactor configuration for electrocatalytic CO₂ reduction: (a) schematic diagram; (b) actual photograph

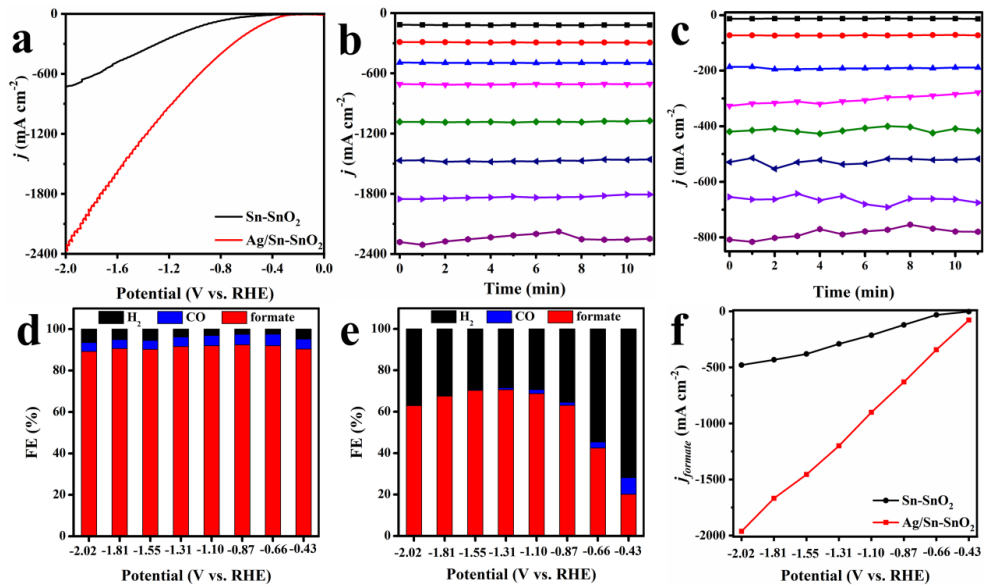


Fig. S24 Electrocatalytic CO₂RR performance in Flow-type reactor using 1M KOH as electrolyte: **(a)** Polarization curves; **(b, c)** Total current densities of Sn-SnO₂ NSs **(b)** and Ag/Sn-SnO₂ NSs **(c)**; **(d, e)** FE for formate, CO and H₂ of Ag/Sn-SnO₂ NSs **(d)** and Sn-SnO₂ NSs **(e)**; **(f)** Partial current densities of formate

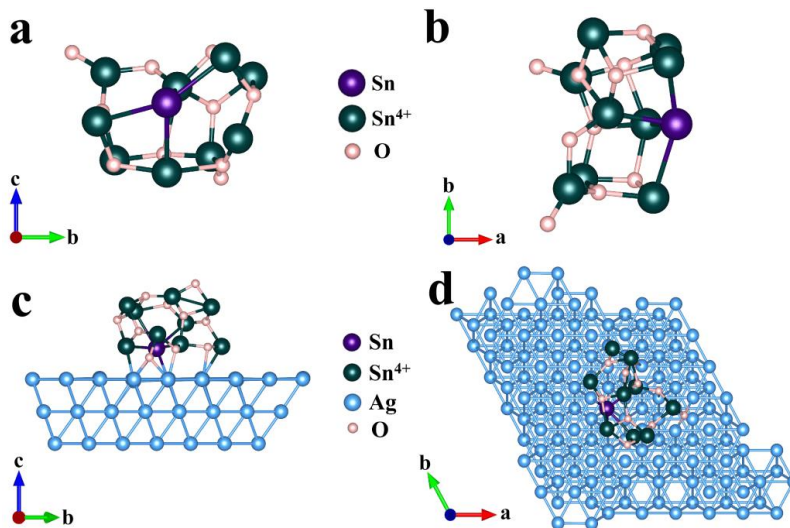


Fig. S25 Side- and top-view of the initial models: **(a, b)** Sn-SnO₂; **(c, d)** Ag/Sn-SnO₂

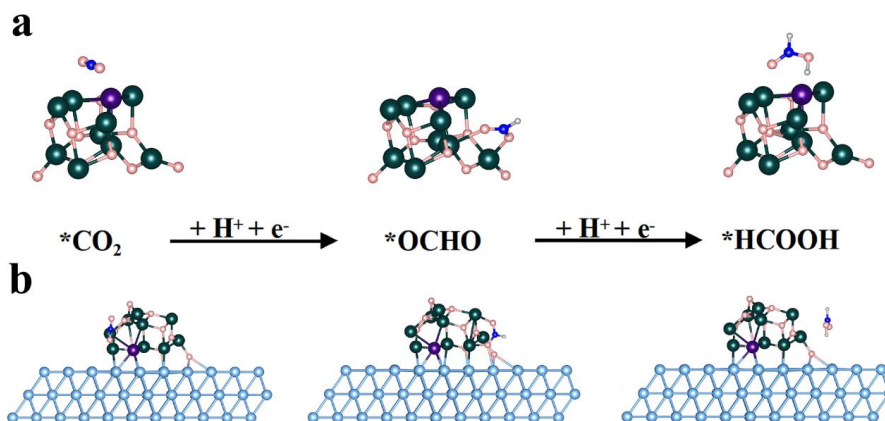


Fig. S26 The optimized intermediate species along the reaction pathways for CO₂ electroreduction to formate on the **(a)** Sn-SnO₂ and **(b)** Ag/Sn-SnO₂

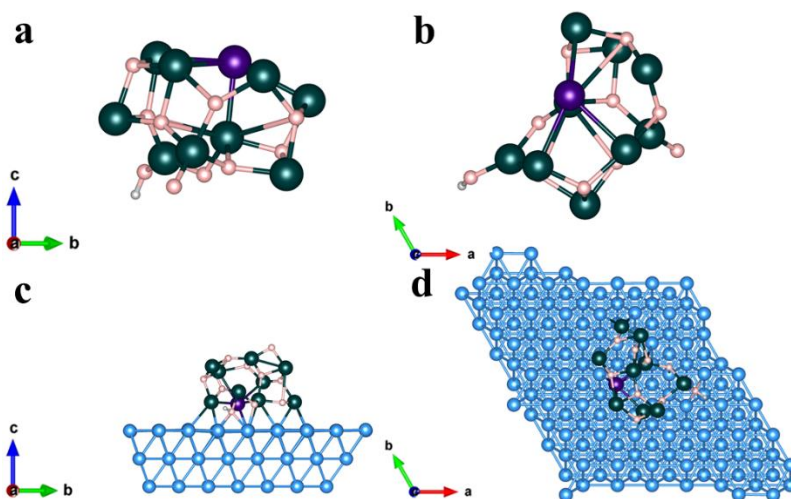


Fig. S27 Calculated adsorption configuration of *H on catalysts: (a, b) Sn-SnO₂; (c, d) Ag/Sn-SnO₂

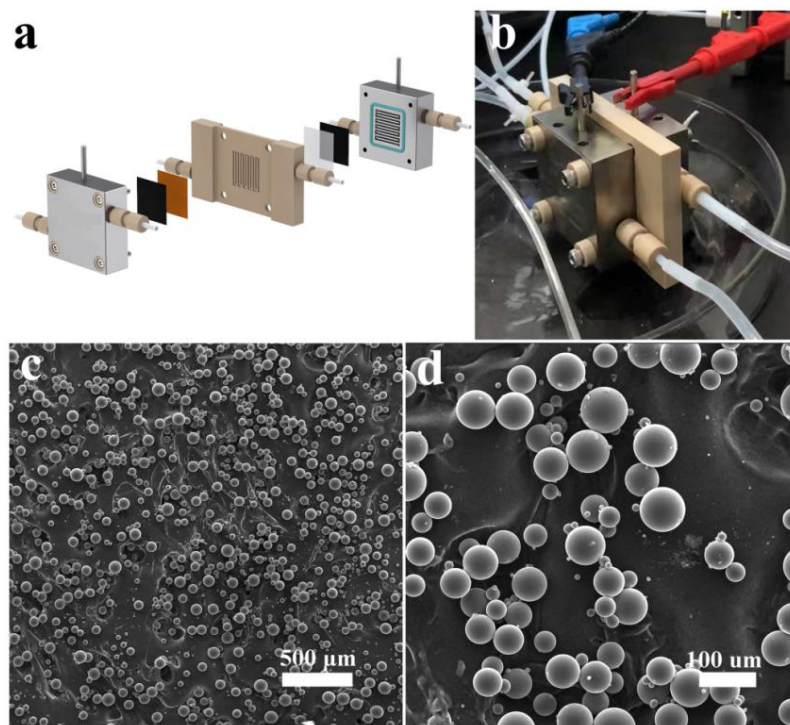


Fig. S28 MEA with PSE layer electrolyzer for pure HCOOH production: (a, b) Schematic diagram, and digital image; (c, d) SEM images of the sulfonated styrene-divinylbenzene copolymer proton conductor

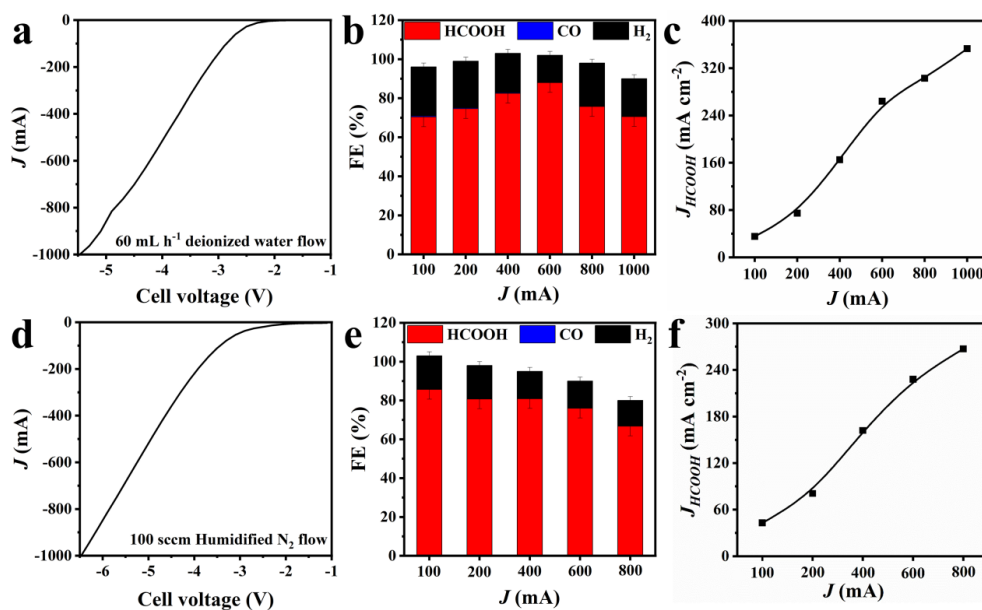


Fig. S29 Electrocatalytic CO₂RR performance of Ag/Sn-SnO₂ NSs in MEA with PSE layer reactor: (a) LSV curve, (b) FE of all products, (c) Partial current densities of HCOOH using DI water as carrier flow; (d) LSV curve, (e) FE of all products, (f) Partial current densities of HCOOH using humidified N₂ as carrier flow

Table S1 Ag K-edge EXAFS fitting results for Ag/Sn-SnO₂, Ag foil, and Ag₂O

sample	shell	N	σ^2 (Å ²)	ΔE_0 (eV)	R (Å)	R-factor
Ag foil	Ag-Ag	12	9.6±0.2	2.0±0.2	2.86±0.00	0.002
Ag ₂ O	Ag-O	4	1.2±1.9	2.0±1.5	2.05±0.01	0.020
Ag/Sn-SnO ₂	Ag-O	1.1±0.2	5.4±5.9	0.9±1.3	2.03±0.01	0.013
	Ag-Ag	2.1±1.1		-8.1±4.1	2.83±0.03	
	Ag-Sn	2.3±1.2		2.92±0.02		

N: Coordination numbers; σ : Debye-Waller parameters, R: coordination distances; R-factor: goodness of fit, ΔE_0 energy shift. S_0^2 is amplitude reduction factor ($S_0^2=0.83$ was obtained by Ag foil fitting and applied for other sample fitting).

Table S2 Sn K-edge EXAFS fitting results for Ag/Sn-SnO₂, Sn-SnO₂, SnO₂, Sn foil, and SnO

sample	shell	N	σ^2 (Å ²)	ΔE_0 (eV)	R (Å)	R-factor
Sn foil	Sn-Sn1	4	10.5±1.0	0.4±0.8	3.00±0.00	0.020
	Sn-Sn2	8	4.9±1.4		3.74±0.07	
SnO ₂	Sn-O	6.5±0.5	1.3±1.3	-1.0±0.9	2.15±0.01	0.017
	Sn-Sn1	1.5±0.5	0.1±2.0	-4.9±2.3	3.17±0.02	
	Sn-Sn2	4.4±1.8	0.1±2.0	4.3±2.1	3.70±0.02	
Sn-SnO ₂	Sn-O	4.7±0.4	1.7±0.9	3.6±1.3	2.05±0.01	0.018
	Sn-Sn1	3.1±0.4		4.4±6.9	3.20±0.04	
	Sn-Sn2	4.0±0.9		3.3±2.1	3.72±0.01	
Ag/Sn-SnO ₂	Sn-O	3.7±0.3	2.8±0.9	3.3±1.8	2.04±0.01	0.018
	Sn-Ag	2.0±0.7		5.8±2.5	3.01±0.02	
	Sn-Sn1	2.1±0.7		3.3±2.1	3.15±0.02	
	Sn-Sn2	3.2±0.9		3.70±0.01		

N: Coordination numbers; σ : Debye-Waller parameters, R: coordination distances; R-factor: goodness of fit, ΔE_0 energy shift. S_0^2 is amplitude reduction factor ($S_0^2=0.88$ was obtained by Sn foil fitting and applied for other sample fitting)

Table S3 Comparison of the catalytic performance of various electrocatalysts for CO₂RR to formate production in H-type reactor

Catalyst	Electrolyte	Potential (V vs. RHE)	j_{formate} (mA cm ⁻²)	FE _{formate} (%)	Reference
Ag/Sn-SnO₂	0.5 M KHCO₃	-1.37	48	90	This work
InSn-3	0.1 M KHCO ₃	-0.9	34.15	86	S1
Cu ₆ Sn ₅ /Sn	0.5 M NaHCO ₃	-1.15	31	70	S2
CuSn-3	0.5 M KHCO ₃	-1.0	26	90	S3
H-SnS ₂	0.1 M KHCO ₃	-1.0	25	87	S4
Ag-Sn/GO	0.5 M NaHCO ₃	-0.94	21.3	88.3	S5
Cu@Sn nanocones	0.5 M NaHCO ₃	-1.1	16	85	S6
Ag-Sn	0.5 M NaHCO ₃	-0.8	16	80	S7
SnO ₂ QWs	0.1 M KHCO ₃	-1.156	13.7	85	S8
SnO _x NPs	0.5 M NaHCO ₃	-1.2	9	80	S9
SnO _x	0.1 M KHCO ₃	-0.75	6.7	80	S10

Table S4 Comparison of the catalytic performances of various electrocatalysts for CO₂RR to formate production in Flow-type reactor

Catalyst	Electrolyte	Potential (V vs. RHE)	j_{formate} (mA cm ⁻²)	FE _{formate} (%)	Stability	Reference
Ag/Sn-SnO₂	1 M KOH	-2.0	2000	90	200 h; 200 mA cm⁻²	This work
Sn-ene QDs	1 M KOH	-2.0	923	89	100 h; 200 mA cm ⁻²	S11
InP QDs	3 M KOH	-2.6	930	90	4 h; 400 mA cm ⁻²	S12
Bi flakes	1 M KOH	-0.7	677	83	6 h; 500 mA cm ⁻²	S13
Bi-ene-NW	1 M KOH	-0.97	570	91	18 h; 200 mA cm ⁻²	S14
ZnIn ₂ S ₄	1 M KOH	-1.0	490	93	60 h; 300 mA cm ⁻²	S15
Bi NSs	1 M KOH	-0.67	400	89	10 h; 197 mA cm ⁻²	S16
Sn _{2.7} Cu	1 M KOH	-0.7	370	84	40 h; 243 mA cm ⁻²	S17
Ni-In ₂ O ₃ @C	1 M KOH	-1.0	350	90	55 h; 200 mA cm ⁻²	S18
FTO/C	1 M KHCO ₃	-1.0	330	90	160 h; 100 mA cm ⁻²	S19
Pits-Bi NS	1 M KOH	-1.5	325	92	110 h; 200 mA cm ⁻²	S20

Table S5 Comparison of the catalytic performances of various electrocatalysts for CO₂RR to pure HCOOH solution in the MEA with PSE layer reactor

Catalyst	j_{total} (mA)	j_{HCOOH} (mA cm ⁻²)	FE _{HCOOH} (%)	Stability (h; mA cm ⁻² ; mol L ⁻¹)	Reference
Ag/Sn-SnO ₂	1000	350	90	200 h; 100 mA cm ⁻² ; 0.14 ^[a]	This work
	800	270	90	25 h; 100 mA cm ⁻² ; 0.27 ^[b]	
In ₂ O ₃ @C	320	80	\	3 h; 30 mA cm ⁻² ; \ ^[a]	S21
2D-Bi	800	200	78	100 h; 30 mA cm ⁻² ; 0.1 ^[a]	S22
Bi MS	220	175	84	110 h; 160 mA cm ⁻² ; 0.13 ^[a]	S23
nBuLi-Bi	800	400	88	100 h; 30 mA cm ⁻² ; 0.1 ^[a]	S24
	300	150	85	30 h; 30 mA cm ⁻² ; 0.35 ^[c]	
Pb ₁ Cu	900	225	90	180 h; 100 mA cm ⁻² ; 0.1 ^[a]	S25
BiSn	250	225	90	12 h; 100 mA cm ⁻² ; 0.41 ^[a]	S26

[a] Formic acid was released by feeding a flow of deionized water (anode-coupled OER reaction); [b, c] Formic acid was released by feeding a flow of N₂ vapour flow (b: anode-coupled OER reaction, c: anode-coupled HOR reaction)

Supplementary References

- [S1] J. Wang, S. Ning, M. Luo, D. Xiang, W. Chen, X. Kang, Z. Jiang, S. Chen, In-Sn alloy core-shell nanoparticles: In-doped SnOx shell enables high stability and activity towards selective formate production from electrochemical reduction of CO₂, Appl. Catal. B: Environ. 288 (2021) 119979. <https://doi.org/10.1016/j.apcatb.2021.119979>
- [S2] Y. Wang, Y. Chen, Y. Zhao, J. Yu, Z. Liu, Y. Shi, H. Liu, X. Li, W. Zhou, Laser-fabricated channeled Cu₆Sn₅/Sn as electrocatalyst and gas diffusion electrode for efficient CO₂ electroreduction to formate. Appl. Catal. B: Environ. 307 (2022) 120991. <https://doi.org/10.1016/j.apcatb.2021.120991>
- [S3] M. Ren, H. Zheng, J. Lei, J. Zhang, X. Wang, B.I. Yakobson, Y. Yao, J.M. Tour, CO₂ to formic acid using Cu-Sn on laser-induced graphene. ACS Appl. Mater. Interfaces 12 (2020) 41223-41229. <https://doi.org/10.1021/acsami.0c08964>
- [S4] A. Zhang, Y. Liang, H. Li, S. Wang, Q. Chang, K. Peng, Z. Geng, J. Zeng, Electronic tuning of SnS₂ nanosheets by hydrogen incorporation for efficient CO₂ electroreduction. Nano Lett. 21 (2021) 7789-7795. <https://doi.org/10.1021/acs.nanolett.1c02757>
- [S5] X. Zhang, F. Li, Y. Zhang, Alan M. Bond, J. Zhang, Stannate derived bimetallic nanoparticles for electrocatalytic CO₂ reduction, J. Mater. Chem. A, 6 (2018) 7851-7858. <https://doi.org/10.1039/C8TA02429D>
- [S6] C. Chen, Y. Pang, F. Zhang, J. Zhong, B. Zhang, Z. Cheng, Sharp Cu@ Sn nanocones on Cu foam for highly selective and efficient electrochemical reduction of CO₂ to formate, J. Mater. Chem. A, 6 (2018) 19621-19630. <https://doi.org/10.1039/C8TA06826G>
- [S7] W. Luc, C. Collins, S. Wang, H. Xin, K. He, Y. Kang, F. Jiao, Ag-Sn bimetallic catalyst with a core-shell structure for CO₂ reduction. J. Am. Chem. Soc. 139 (2017) 1885-1893. <https://doi.org/10.1021/jacs.6b10435>

- [S8] S. Liu, J. Xiao, X.F. Lu, J. Wang, X. Wang, X.W. Lou, Efficient electrochemical reduction of CO₂ to HCOOH over sub-2 nm SnO₂ quantum wires with exposed grain boundaries. *Angew. Chem. Inter. Ed.* 58 (2019) 8499-8503. <https://doi.org/10.1002/anie.201903613>
- [S9] M.K. Kim, H. Lee, J.H. Won, W. Sim, S.J. Kang, H. Choi, M. Sharma, H.S. Oh, S. Ringe, Y. Kwon, H.M. Jeong, Design of less than 1 nm scale spaces on SnO₂ nanoparticles for high-performance electrochemical CO₂ reduction. *Adv. Funct. Mater.* 32 (2021) 2107349. <https://doi.org/10.1002/adfm.202107349>
- [S10] Y. Cheng, J. Hou, P. Kang, Integrated capture and electroreduction of flue gas CO₂ to formate using amine functionalized SnOx nanoparticles. *ACS Energy Lett.* 6 (2021) 3352-3358. <https://doi.org/10.1021/acsenergylett.1c01553>
- [S11] M. Zhang, S. Zhou, W. Wei, D.-D. Ma, S.-G. Han, X. Li, X.-T. Wu, Q. Xu, Q.-L. Zhu, Few-atom-layer metallene quantum dots toward CO₂ electroreduction at ampere-level current density and Zn-CO₂ battery. *Chem Catal.* 2 (2022) 3528-3545. <https://doi.org/10.1016/j.checat.2022.10.001>
- [S12] I. Grigioni, L.K. Sagar, Y.C. Li, G. Lee, Y. Yan, K. Bertens, R.K. Miao, X. Wang, J. Abed, D.H. Won, F.P. García de Arquer, A.H. Ip, D. Sinton, E.H. Sargent, CO₂ electroreduction to formate at a partial current density of 930 mA cm⁻² with InP colloidal quantum dot derived catalysts. *ACS Energy Lett.* 6 (2020) 79-84. <https://doi.org/10.1021/acsenergylett.0c02165>
- [S13] Z. Xing, X. Hu, X. Feng, Tuning the microenvironment in gas-diffusion electrodes enables high-rate CO₂ electrolysis to formate. *ACS Energy Lett.* 6 (2021) 1694-1702. <https://doi.org/10.1021/acsenergylett.1c00612>
- [S14] M. Zhang, W. Wei, S. Zhou, D.-D. Ma, A. Cao, X.-T. Wu, Q.-L. Zhu, Engineering a conductive network of atomically thin bismuthene with rich defects enables CO₂ reduction to formate with industry-compatible current densities and stability, *Energy Environ. Sci.* 14 (2021) 4998-5008. <https://doi.org/10.1039/D1EE01495A>
- [S15] L.P. Chi, Z.Z. Niu, X.L. Zhang, P.P. Yang, J. Liao, F.Y. Gao, Z.Z. Wu, K.B. Tang, M.R. Gao, Stabilizing indium sulfide for CO₂ electroreduction to formate at high rate by zinc incorporation. *Nat. Commun.* 12 (2021) 5835. <https://doi.org/10.1038/s41467-021-26124-y>
- [S16] J. Yang, X. Wang, Y. Qu, X. Wang, H. Huo, Q. Fan, J. Wang, L. M. Yang, Y. Wu, Bi-based metal-organic framework derived leafy bismuth nanosheets for carbon dioxide electroreduction. *Adv. Energy Mater.* 10 (2020) 2001709. <https://doi.org/10.1002/aenm.202001709>
- [S17] K. Ye, Z. Zhou, J. Shao, L. Lin, D. Gao, N. Ta, R. Si, G. Wang, X.J.A.C.I.E. Bao, In situ reconstruction of a hierarchical Sn-Cu/SnOx core/shell catalyst for high-performance CO₂ electroreduction. *Angew. Chem. Int. Ed.* 59 (2020) 4814-4821. <https://doi.org/10.1002/anie.201916538>
- [S18] Z. Chen, G. Yu, B. Li, X. Zhang, M. Jiao, N. Wang, X. Zhang, L. Liu, In situ carbon encapsulation confined nickel-doped indium oxide nanocrystals for boosting CO₂ electroreduction to the industrial level. *ACS Catal.* 11 (2021) 14596-14604. <https://doi.org/10.1021/acscatal.1c04182>
- [S19] Y.J. Ko, J.Y. Kim, W.H. Lee, M.G. Kim, T.Y. Seong, J. Park, Y. Jeong, B.K. Min, W.S. Lee, D.K. Lee, H.S. Oh, Exploring dopant effects in stannic oxide nanoparticles

- for CO₂ electro-reduction to formate. *Nat. Commun.* 13 (2022) 2205.
<https://doi.org/10.1038/s41467-022-29783-7>
- [S20] Y. Yuan, Q. Wang, Y. Qiao, X. Chen, Z. Yang, W. Lai, T. Chen, G. Zhang, H. Duan, M. Liu, H. Huang, In situ structural reconstruction to generate the active sites for CO₂ electroreduction on bismuth ultrathin nanosheets. *Adv. Energy Mater.* 12 (2022) 2200970. <https://doi.org/10.1002/aenm.202200970>
- [S21] Z. Wang, Y. Zhou, D. Liu, R. Qi, C. Xia, M. Li, B. You, B.Y. Xia, Carbon-confined indium oxides for efficient carbon dioxide reduction in a solid-state electrolyte flow cell. *Angew. Chem. Inter. Ed.* 61 (2022) e202200552.
<https://doi.org/10.1002/anie.202200552>
- [S22] C. Xia, P. Zhu, Q. Jiang, Y. Pan, W. Liang, E. Stavitski, H.N. Alshareef, H. Wang, Continuous production of pure liquid fuel solutions via electrocatalytic CO₂ reduction using solid-electrolyte devices. *Nat. Energy* 4 (2019) 776-785.
<https://doi.org/10.1038/s41560-019-0451-x>
- [S23] Y. Zhang, R. Zhang, F. Chen, F. Zhang, Y. Liu, X. Hao, H. Jin, X. Zhang, Z. Lu, H. Dong, F. Lu, W. Wang, H. Liu, Y. Chen, Mass-transfer-enhanced hydrophobic Bi microsheets for highly efficient electroreduction of CO₂ to pure formate in a wide potential window. *Appl Catal B: Environ* 322 (2023) 122127.
<https://doi.org/10.1016/j.apcatb.2022.122127>
- [S24] L. Fan, C. Xia, P. Zhu, Y. Lu, H. Wang, Electrochemical CO₂ reduction to high-concentration pure formic acid solutions in an all-solid-state reactor. *Nat. Commun.* 11 (2020) 3633. <https://doi.org/10.1038/s41467-020-17403-1>
- [S25] T. Zheng, C. Liu, C. Guo, M. Zhang, X. Li, Q. Jiang, W. Xue, H. Li, A. Li, C.-W. Pao, J. Xiao, C. Xia, J. Zeng, Copper-catalysed exclusive CO₂ to pure formic acid conversion via single-atom alloying. *Nat. Nanotech.* 16 (2021) 1386-1393.
<https://doi.org/10.1038/s41565-021-00974-5>
- [S26] L. Li, Z. Liu, X. Yu, M. Zhong, Achieving high single-pass carbon conversion efficiencies in durable CO₂ electroreduction in strong acids via electrode structure engineering. *Angew. Chem. Inter. Ed.* 15 (2023) e202300226.
<https://doi.org/10.1002/anie.202300226>